Nucleic Acids Research, 1998, Vol. 26, No. 11 **2779–2788**

Structural features of the minimal DNA binding domain (M98–F219) of human nucleotide excision repair protein XPA

Garry W. Buchko, Shuisong Ni, Brian D. Thrall and Michael A. Kennedy*

Pacific Northwest National Laboratories, Environmental Molecular Sciences Laboratory and Molecular Biosciences Department, Richland, WA 99352, USA

Received December 22, 1997; Revised and Accepted April 16, 1998

ABSTRACT

XPA, an essential protein in nucleotide excision repair (NER), interacts with damaged DNA and other proteins (RPA, ERCC1 and TFIIH) to remove a wide variety of chemically and structurally distinct DNA lesions from the eukaryotic genome. To understand the structural basis for the role of XPA in the repair process, the structure of the minimal DNA binding domain of human XPA [XPA-MBD (M98–F219)] was studied by NMR spectroscopy. A three-dimensional structure for XPA-MBD was generated using distance geometry and simulated annealing methods from NOE-based distance restraints, hydrogen bond and Zn–S distance restraints, and dihedral restraints. The structure calculations indicate that XPA-MBD contains elements of well-defined secondary structure interspaced with disordered loops organized into two non-interactive sub-domains: a zinc-binding core (D101–K137) and a loop-rich domain (L138–F219). The zinc-associated core contains an antiparallel β-sheet (Y102–C105 and K110–M113) and an α-helix (C126–K137) separated by a poorly defined turn, reminiscent of the structure of the zinc-binding domain of the chicken erythroid transcription factor GATA-1 when bound to its cognate DNA sequence. The loop-rich domain contains a triple-strand antiparallel β-sheet (L138–T140, L182–M178 and K163–K167), three loops (K151–L162, N169–D177 and Q208–F219) and three α-helices (K141–L150, K183–W194 and Q197–R207). The XPA-MBD structure is discussed in terms of known functions: binding single- and double-stranded DNA and binding RPA.

INTRODUCTION

Nucleotide excision repair (NER) is an important cellular mechanism, conserved from yeast to humans, for eliminating many structurally distinct DNA lesions from the genome (1–7). The process involves five steps: recognition, incision, excision, resynthesis and ligation. In mammalian cells the incision usually occurs by hydrolysis of the fifth phosphodiester bond 3′ to the lesion and the 24th phosphodiester bond 5′ to the lesion (8). The single-stranded fragment containing the damaged DNA is excised, the unmodified strand is used as a template to resynthesis the excised DNA, and DNA ligase seals the nicks.

Mutations in NER genes are responsible for at least three human cancer-prone genetic instability syndromes: trichothiodystrophy, Cockayne's syndrome and xeroderma pigmentosum (XP) (9). The latter is an autosomal recessive disease often characterized by hypersensitivity to sunlight, elevated levels of skin cancer and neurological abnormalities. Systematic complementation analysis by cell fusion techniques has identified seven XP complementation groups (A–G) and a variant form (9). Five of the relevant gene products (XP-A, XP-B, XP-C, XP-D and XP-G mutations) have been identified (10–16) and are believed to work together in NER. Among the complementation groups, XP-A is the most common and most severe form of the disease (9), with at least 12 different sites of mutation identified in the XPA gene (17). The human XPA gene product, a 31 kDa protein (XPA) of 273 amino acids (18), has no inherent catalytic activity yet plays a central role in NER. XPA has been reported to interact specifically with other NER proteins, including ERCC1 (19,20), TFIIH (21,22) and RPA (23), and to have a greater affinity for DNA damaged by UV, cisplatin and osmium tetroxide than for undamaged DNA (24–26). While many chemically and structurally distinct DNA lesions generated by a broad variety of physical and chemical DNA damaging agents, including natural toxins, man-made carcinogens and UV and ionizing radiation (4,27,28) are repaired by NER, the mechanism of the XPA-DNA interactions is unknown. Instead of recognizing the structure of specific DNA lesions, the prevailing hypothesis is that XPA responds to distortions in the normal DNA topology (6,25,29); DNA damage recognition being facilitated by lesions that produce single-stranded character leading to an 'open complex formation'. DNA damage recognition is also facilitated by interactions with other proteins. The association of RPA with XPA leads to the formation of a complex which binds UV-irradiated DNA with a greater affinity than either protein alone and leads to an expansion of the types of lesions recognized by NER (30).

The location of the DNA binding domain of XPA has been pinpointed to a 122 amino acid region between M98 and F219 that contains a class IV, C4-type zinc-binding motif; $C105–X_2–C108–X_{17}–C126–X_2–C129$ (where X is a variable amino acid) (31). Zinc-binding domains play a major role in eukaryotic protein–nucleic acid interactions (32,33) and it is an essential functional motif in XPA because the replacement of C105, C108, C126 or C129 with a Ser severely reduces NER activity (17). Proton NMR solution studies of a synthetic 41 residue peptide

*To whom correspondence should be addressed. Tel: +1 509 372 2168; Fax: +1 509 376 2303; Email: ma_kennedy@pnl.gov

containing the zinc-binding region [zXPA-41 (D101–K141)] (34) suggest that zXPA-41 adopts a structure similar to the DNA binding domain of the chicken erythroid transcription factor GATA-1 bound to its cognate DNA target sequence (35). Although the zinc-binding core structures of XPA and cGATA-1 appear similar (34,35), the motif in cGATA-1 requires only 28 additional C-terminal residues to bind DNA, while XPA requires an additional 82 C-terminal residues (31). The ^{15}N, $^{13}C^{\alpha}$, ^{13}CO, $^{1}H^{N}$ and $^{1}H^{\alpha}$ backbone resonances of XPA-MBD have been previously assigned (36). To better understand how XPA is involved in NER, the majority of the side-chain proton resonances of the 122 residue minimal DNA binding domain of XPA (M98–F219) have been assigned and the three-dimensional structure determined using multi-dimensional NMR protocols (37).

MATERIALS AND METHODS

Preparation of $^{15}N/^{13}C$ labelled XPA-MBD

The cDNA for human XPA residues M98–F219 (XPA-MBD) was cloned into the vector pET-11d and transfected into the host *Escherichia coli* bacterial strain BL21(DE3)pLysS (Novagen Inc., Madison, WI). Cells were grown at 37°C to an OD_{600} reading of 0.6–0.8 in minimal medium (Miller) containing 100 µg/ml ampicillin (Sigma, St Louis, MO), 34 µg/ml chloramphenicol (Fluka BioChemika, Switzerland), $^{15}NH_4Cl$ (Cambridge Isotopes Inc., Woburn, MA) and [$^{13}C_6$]-D-glucose (Cambridge Isotopes Inc., Woburn, MA). The medium was then supplemented to a final concentration of 0.01 mM zinc acetate (Sigma), the temperature lowered to 28°C, and protein expression induced for 3–5 h with 1.0 mM isopropyl-1-thio-β-D-galactopyranoside (Sigma). Cells were harvested by centrifugation for 15 min at 5000 *g* at 4°C and resuspended in 50 mM Tris–HCl (Sigma), pH 7.5. Phenylmethylsulfonyl fluoride (0.2 mM; Sigma) was added to the cell suspension immediately prior to lysis by three passes through a French Press (SLM Instruments Inc., Rochester, NY). The debris was removed by centrifugation at 50 000 *g* for 30 min in a SW-50 rotor and the supernatant applied to a POROS HQ/M strong anion exchange column attached to a BioCAD Sprint Perfusion Chromatography System (PerSeptive Biosystems, Framingham, MA). The column was washed with 50 mM Tris–HCl, 50 mM Bis–Tris–propane (Sigma), pH 8.0 and eluted in the same buffer with a linear gradient of 0.0–0.25 mM NaCl over 15 column volumes. The major chromatogram peak was collected, pooled and then concentrated with a Centriprep-10 (Amicon Inc., Beverly, MA). Sample purity was >90% as determined by SDS–polyacrylamide gel electrophoresis and Coomassie Blue staining. Western blot analysis of the purified protein using a polyclonal XPA antibody (Santa Cruz Biotechnology, CA) tested positive. DNA filter binding assays indicated that the isolated XPA-MBD was active, having a 12-fold greater affinity for cisplatin-damaged DNA over undamaged DNA (linearized pUC19 plasmid). Analysis on a TSK-GEL G3000SW_{XL} (7.8 mm × 30 cm, 5 µm) size-exclusion column (50 mM K_2PO_4, 200 mM NaCl pH 7.0) showed one band with a molecular weight expected for a monomeric 15 kDa protein. Mass determination of XPA-MBD by electrospray ionization mass spectral analysis of a non-labelled preparation [Finnigan TSQ 7000 triple-quadrupole mass spectrometer, (San Jose, CA)], confirmed the predicted molecular weight for a protein containing a 1:1 stoichiometric ratio of zinc. Zinc K-edge extended X-ray absorption fine structure (EXAFS) spectra collected on a lyophilized sample confirmed the coordination of zinc with four sulfur atoms (38). The final yield of XPA-MBD obtained from the soluble fraction was ~60 mg/l.

Table 1. Acquisition parameters for NMR experiments (^{1}H = 750 MHz) on XPA-MBD

Experiment	Nucleus			No. of complex pts.			Spectral width (Hz)		
	F1	F2	F3	F1	F2	F3	F1	F2	F3
HSQC	^{1}H	^{15}N		1024	28		10000	1350	
NOESY-HMQC	^{1}H	^{1}H	^{15}N	1536	128	48	9000	9000	2100
C-NOESY-HMQC*	^{1}H	^{1}H	^{13}C	1024	32	27	6500	5000	3000
HNCA	^{1}H	^{13}C	^{15}N	1024	25	32	9000	5640	2100
CBCA(CO)NH	^{1}H	^{13}C	^{15}N	1024	45	25	9000	11280	1350
HNCACB	^{1}H	^{13}C	^{15}N	1024	50	30	9000	11280	2100
HNCO	^{1}H	^{13}C	^{15}N	1024	50	32	9000	2265	1350
HCCH_TOCSY	^{1}H	^{1}H	^{13}C	1024	128	38	9000	6750	4527
HCCH-TOCSY-NNH	^{1}H	^{1}H	^{15}N	1024	48	27	9000	7400	2100
J-resolved HMQC*	^{1}H	^{15}N		3200	800		6400	1600	

*Performed at a ^{1}H resonance frequency of 500 MHz.

NMR spectroscopy

A 1.5 mM sample of XPA-MBD was prepared in 600 µl of 90% H_2O/10% D_2O in the following buffer: 20 mM K_2HPO_4, 100 mM KCl, 25 mM perdeuterated dithiothreitol, 50 µM zinc acetate, 50 µM NaN_3, pH 7.3. Two-dimensional $^{15}N/^{1}H$ HSQC (39,40) and three-dimensional HNCA (41), ^{15}N-edited NOESY-HMQC (Varian, Palo Alto, CA), ^{13}C-edited NOESY-HMQC (Varian), CBCA(CO)NH (42), HNCACB (42), HNCO (42), HCCH-TOCSY (43) and HCCH-TOCSY-NNH (44) data were all collected at 30°C on a Varian 750- or 500-Unityplus spectrometer equipped with a triple-resonance $^{1}H/^{13}C/^{15}N$ probe and a gradient amplifier. The parameters used for data collection are listed in Table 1. The data were processed with Felix95 (MSI, San Diego, CA) software. Sequence-specific backbone resonance assignments (^{15}N, $^{13}C^{\alpha}$, ^{13}CO, $^{1}H^{N}$ and $^{1}H^{\alpha}$) for XPA-MBD have been reported previously (36). Subsequently, most of the side-chain proton resonances have been assigned and an updated table containing the ^{15}N, $^{13}C^{\alpha}$, $^{13}C^{\beta}$, ^{13}CO, $^{1}H^{N}$, $^{1}H^{\alpha}$, $^{1}H^{\beta}$, $^{1}H^{\gamma}$, $^{1}H^{other}$ chemical shifts are available as Supplementary Material. In order to identify slowly exchanging amide protons, a ^{15}N-labelled sample of XPA-MBD in 90% H_2O/10% D_2O (600 µl) was exchanged into 98% D_2O on a Pharmacia PD-10 size-exclusion column packed with Sephedex-G25 media pre-treated (six column volumes) with NMR buffer prepared in 98% D_2O (pH meter reading of 7.0). The protein was collected in one 600 µl fraction (gravity elution) with the addition of three column volumes of deuterated buffer. $^{15}N/^{1}H$ HSQC spectra (18 min) were recorded at 1, 2 and 4 h. Amide resonances still present after 1 h are identified by an open circle in Figure 1. In order to obtain semi-quantitative $^{3}J_{^{1}H^{N},^{1}H^{\alpha}}$ values, a $^{15}N/^{1}H$ HMQC J-resolved spectrum (45) was collected and processed with a 90° shifted sine-bell function in D1 and a 20° shifted sine-bell function in D2. Coupling constants >6.5 Hz are identified by an open box in Figure 1.

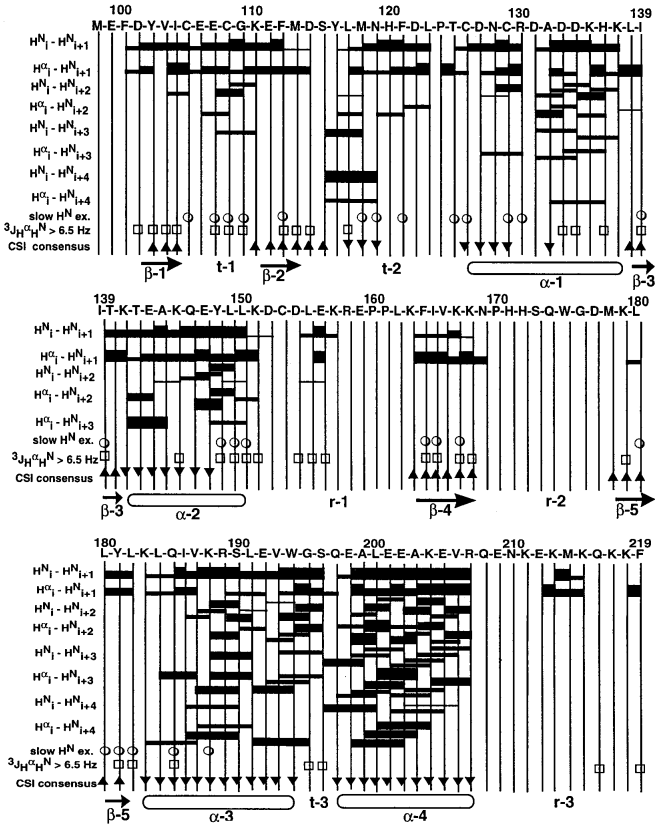

Figure 1. Summary of the short- and medium-range NOEs, slowly exchanging backbone amide protons, $^{3}J_{1HN,1H\alpha}$ coupling constants and consensus CSIs for XPA-MDB at 30°C, pH 7.3. The NOE intensities are proportional to the height of the bars. Open circles indicate slowly exchanging $^{1}H^{N}$ resonances (>1 h). Open squares indicate $^{3}J_{1HN,1H\alpha}$ coupling constants >6.5 Hz. Upright triangles represent a β-strand consensus CSI and inverted triangles represent an α-helix consensus CSI. Predicted elements of secondary structure are depicted by arrows for β-strands and ovals for α-helices.

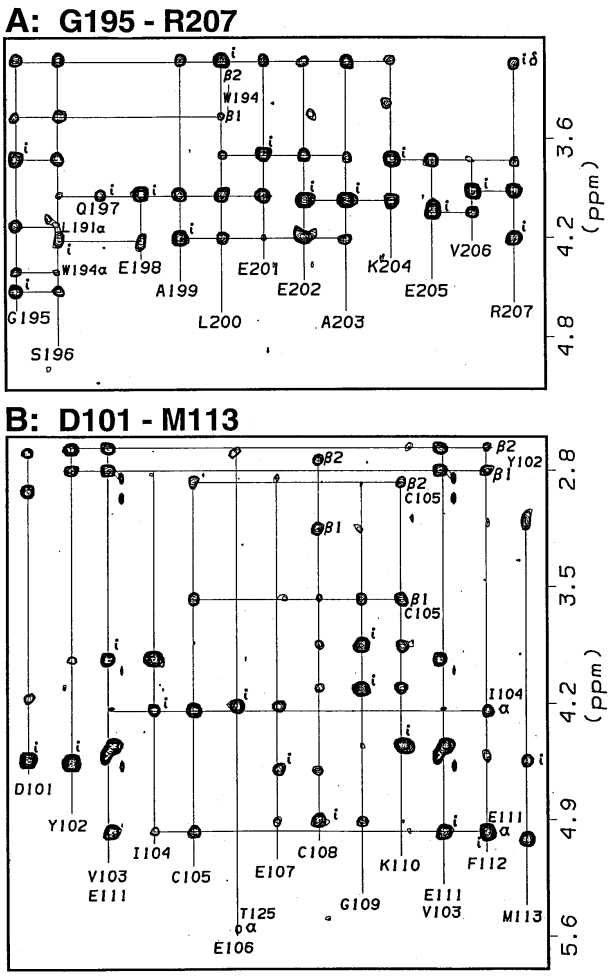

Figure 2. Strip plots extracted from the τ_m = 150 ms ^{15}N-edited NOESY-HMQC spectrum of XPA-MBD illustrating $^{1}H^{N}$ to $^{1}H^{\alpha}$ NOEs for residues G195–R207 (**A**) and D101–M113 (**B**). The $^{1}H^{\alpha}$–$^{1}H^{N}$ cross peaks are labeled with an 'i'. Note that the $^{1}H^{N}$ strips for V103 and E111 are the same.

Tertiary structure calculations for XPA-MBD

Because of the absence of assignable long-range NOEs between the N- and C-terminal regions, and the paucity of NOEs within residues Q208–F219, distance geometry/simulated annealing structure calculations [DGII program of Insight95 (MSI, San Diego, CA)] (46) for XPA-MBD were divided into two parts, M98–L139 and H136–Q208. The initial distance restraints were obtained by classifying the NOE peak volumes from the ^{15}N-edited and ^{13}C-edited NOESY-HMQC experiments into strong (1.80–2.5 Å), medium (2.50–3.50 Å) and weak (3.50–5.00 Å) bins. Following the generation of ten distance geometry/simulated annealing derived structures, the distance restraints were either widened or eliminated to reflect uncertainty in the distance classification or the integration of overlapping cross peaks. The process was repeated until no distance violations >0.1 Å were observed. An average structure for both domains was generated from an ensemble of 4 out of 10 calculated structures after minimization (250 steps conjugant gradient) which included tighter omega dihedral restraints (–178 to 178° versus –176 to 176°). A final set of 378 ^{1}H–^{1}H NOE-based distance restraints (174 inter residue), 10 hydrogen bond restraints and 16 ϕ dihedral restraints were used in the distance geometry/simulated annealing calculations for M98–L139. Ten additional distance restraints were used to constrain the zinc coordination to a tetrahedral geometry [six S–S distance ranges of 3.60–3.85 Å and four Zn–S distance ranges of 2.30–2.40 Å (35,38)] about the sulfur atoms of C105, C108, C126 and C129. For the C-terminal region, a final set of 656 ^{1}H–^{1}H NOE-based distance restraints (299 inter residue), 20 hydrogen bond restraints and 36 ϕ dihedral restraints were used in the distance geometry/simulated annealing calculations.

RESULTS

Two-dimensional ^{15}N/^{1}H HSQC spectra of XPA-MBD contain a wide chemical shift dispersion of the amide proton resonances (~4 p.p.m.) (42) characteristic of a non-random protein conformation. Out of the 117 potentially observable $^{1}H^{N}$ backbone resonances (122 minus four prolines and terminal amide), 104 resonances were observed in the ^{15}N/^{1}H HSQC spectrum and 100 of these were previously assigned (85%) (36). Using additional three-dimensional NMR experiments, most of the side-chain ^{1}H resonances of the 100 identified $^{1}H^{N}$ XPA-MBD resonances were subsequently assigned (see Supplementary

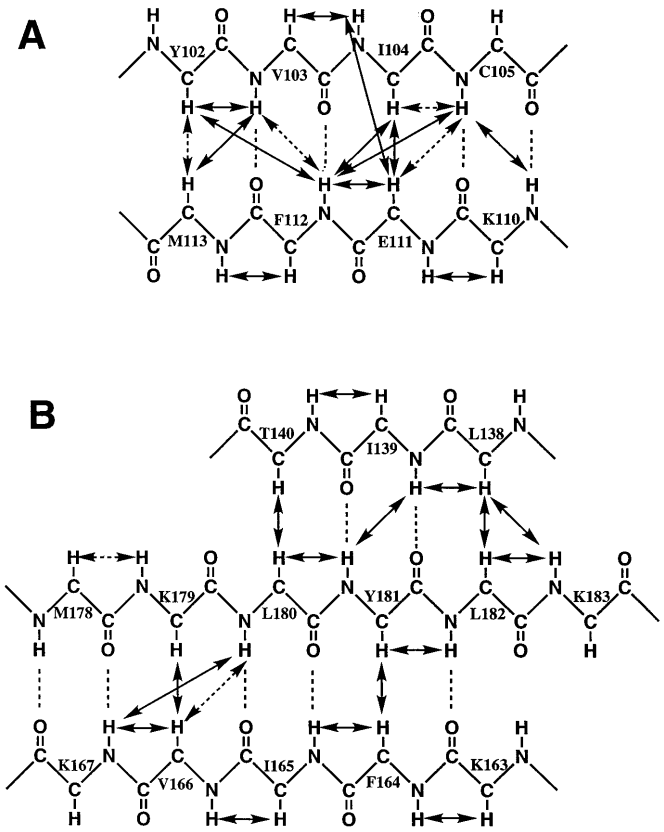

Figure 3. Summary of the NOEs across (**A**) the antiparallel β-sheet between Y102–C105 (β-1) and K110–M113 (β-2) and (**B**) the antiparallel triple-strand β-sheet between L138–T140 (β-3), M178–K183 (β-5) and K167–K163 (β-4). The unambiguous NOEs are illustrated by solid arrows. NOEs shown with dashed arrows could not be confirmed unambiguously due to degeneracies. Hydrogen bonds supported by amide protons that slowly exchange in D_2O are indicated by dashed lines.

Material). Attempts to observe absent amide resonances by lowering the pH below 7.0 to increase the $^1H^N$ lifetimes resulted in the denaturation of the protein in the time required to execute the three-dimensional NMR experiments.

Figure 1 summarizes (i) the short- and medium-range ^1H–^1H NOE data involving $^1H^\alpha$ and $^1H^N$ protons obtained from the ^{15}N-edited NOESY-HMQC spectrum, (ii) slowly exchanging $^1H^N$ resonances following exchange of the sample into a D_2O based buffer, (iii) $^3J_{^1H^N,^1H^\alpha}$ coupling constants obtained from a J-resolved $^{15}N/^1H$ HMQC spectrum and (iv) the regions of α-helix and β-sheet predicted by the consensus CSI using $^{13}C^\alpha$, $^{13}C^\beta$, ^{13}CO and $^1H^\alpha$ chemical shifts (47,48). The elements of secondary structure determined from the NMR data are also illustrated in Figure 1: four α-helices (α-1 to α-4), five β-strands (β-1 to β-5), three turns (t-1 to t-3) and three disordered loops (r-1 to r-3). Because of the presence of three loops in the C-terminal region (L138–F219) we call this the loop-rich domain (for simplicity we also refer to r-3 in XPA-MBD as a loop, although it is not bound to a secondary structure motif). Note that 15 out of the 17 absent $^1H^N$ resonances are in the disordered loops suggesting substantial conformational exchange in these regions.

XPA-MBD contains four helical regions: C126–K137 (α-1), K141–L150 (α-2), K183–W194 (α-3) and Q196–R207 (α-4). The helices were identified by characteristic patterns of NOEs (49) and negative consensus CSI (Fig. 1). Strip plots extracted from the ^{15}N-edited NOESY-HMQC spectrum, shown in Figure 2A, illustrate the quality of the NMR data and the typical helical NOE network of $^1H^\alpha_i$ to i+1, i+2, i+3 and i+4 $^1H^N$ cross peaks that extend throughout α-4. No medium-range sequential $^1H^\alpha_i$ to $^1H^N_{i+1\ (\text{or greater})}$ NOEs were observed between α-3 and α-4, suggesting a very tight turn, or 'kink', centered at G195–S196 (t-3). Glycine residues are known to disrupt helices (50) and non-helical $^3J_{^1H^N,^1H^\alpha}$ values >6.5 Hz for G195 and S196 further support a helical break between α-3 and α-4. A number of long-range NOEs were observed between α-3 and α-2 and between α-4 and α-2, such as those between the epsilon ring proton of W195 and the methyl groups of L149 and L150, indicating that hydrophobic interactions force the three helices into a bundle.

Five β-strands are found in XPA-MBD: Y102–C105 (β-1), K110–M113 (β-2), L138–T140 (β-3), K163–K168 (β-4) and M178–L182 (β-5). NOE patterns typical of a β-sheet structure, such as a weak $^1H^\alpha_i$ to $^1H^N_i$ cross peak accompanied with a strong sequential $^1H^\alpha_i$ to $^1H^N_{i+1}$ cross peak (49), are evident in the strip plots extracted from the ^{15}N-edited NOESY-HMQC spectrum for D101–M113 in Figure 2B. Figure 3A summarizes the sequential NOEs and the long range interstrand $^1H^\alpha_i$ to $^1H^N_j$, $^1H^N_i$ to $^1H^N_j$, and H^α_i to $^1H^\alpha_j$ NOEs, used to define the antiparallel β-sheet between β-1 and β-2. The β-sheet is corroborated in the D_2O exchange experiment by the observation of four slowly exchanging $^1H^N$ resonances for residues that are predicted to form hydrogen bonds between β-1 and β-2. Sixteen unambiguous NOEs observed among the other three β-strands, summarized in Figure 3B, were used to identify a triple-stranded antiparallel β-sheet centered about β-5. NOEs that uniquely identify the antiparallel nature of the second β-sheet include strong $^1H^\alpha_i$ to $^1H^\alpha_j$ NOEs between K179 and V166, Y181 and F164, L182 and L138 and L180 and T140. Seven slowly exchanging $^1H^N$ resonances in positions where hydrogen bonds are predicted between β-3, β-5 and β-4 further corroborate the second β-sheet.

The elements of secondary structure obtained from the data in Figure 1 were introduced into the starting structures for the distance geometry/simulated annealing calculations carried out independently on the two sub-domains, M98–L138 and H136–Q208. The convergence of the final set of calculated structures for each sub-domain is illustrated in Figure 4. Figure 4A and B is a superposition of the N–C^α–C=O backbone atoms of the final ensemble of calculated structures on the average structure

Figure 4. Confomational ensembles of calculated structures for the zinc-binding core (**A**) and loop-rich domain (**B**) of XPA-MBD superimposed on the average structure (highlighted). Superimposed are the backbone atoms (N–C^α–C=O) of residues F100–M113 and C126–K137 in (A) (RMSD on mean = 1.5 ± 0.3) and residues I139–K151, K163–K167 and M178–R207 in (B) (RMSD on mean = 1.6 ± 0.3). (C and D) Ribbon representations of the backbone of the average structure of the zinc-binding core (**C**) and the loop-rich domain (**D**) of XPA-MBD. The four Cys residues that chelate the zinc are highlighted in (D). Red, α-helix; yellow, β-sheet; blue, turn; green, random coil.

A

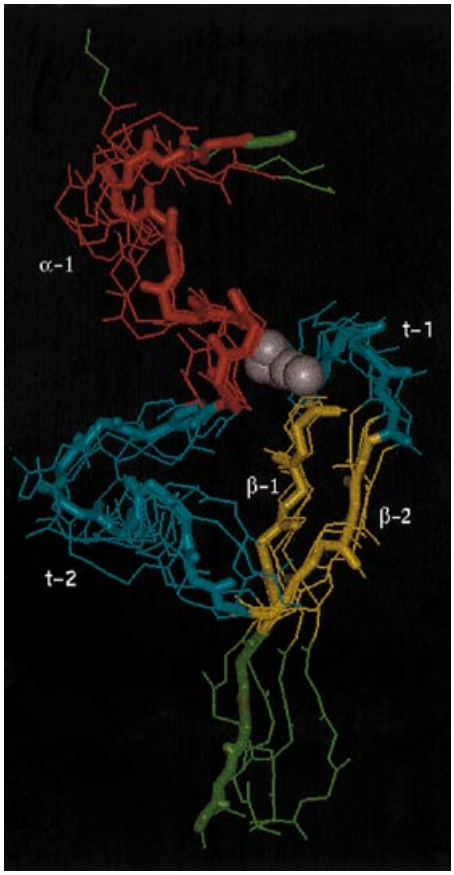
α-1
t-1
β-1
β-2
t-2

B

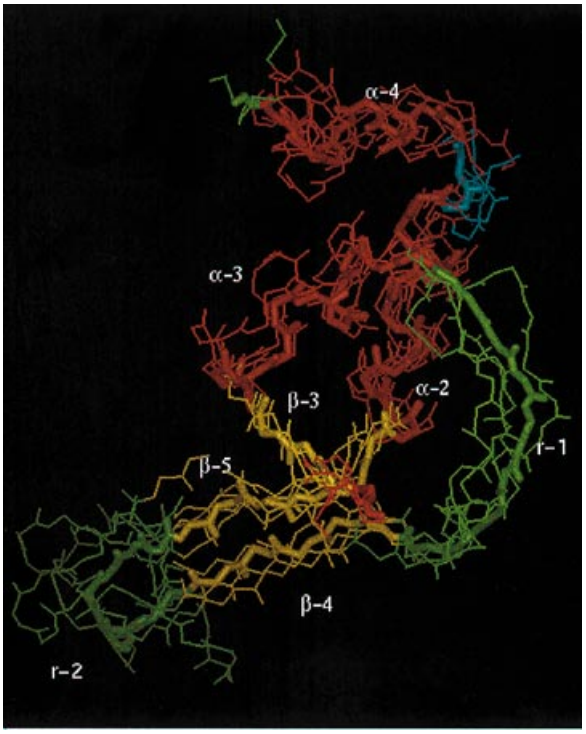
α-4
α-3
α-2
β-3
r-1
β-5
β-4
r-2

C

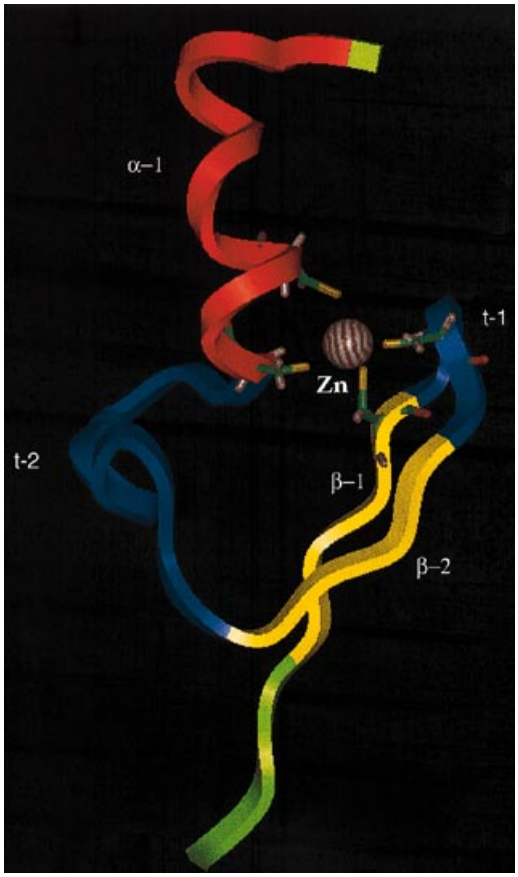
α-1
t-1
Zn
t-2
β-1
β-2

D

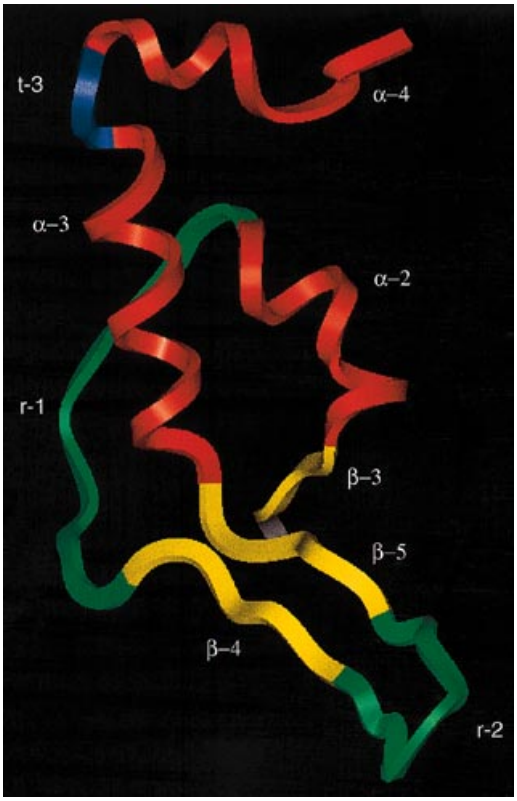
t-3
α-4
α-3
α-2
r-1
β-3
β-5
β-4
r-2

Table 2. Backbone atom RMS differences (Å) for the final set of calculated structures of the zinc-binding core and loop-rich domain of XPA-MBD

β-strand	RMSD	β-sheet	RMSD	α-helix	RMSD	turns	RMSD
βI	0.21 ± 0.06	β-1/β-2	0.45 ± 0.06	α-1	1.3 ± 0.3	t-1	0.34 ± 0.17
β-2	0.39 ± 0.06					t-2	1.2 ± 0.4
β-3	0.20 ± 0.06	β-3/β-5/β-4	1.08 ± 0.30	α-2	0.52 ± 0.28	t-3	0.56 ± 0.20
β-4	0.85 ± 0.26			α-3	0.65 ± 0.18		
β-5	0.81 ± 0.08			α-4	1.8 ± 0.3		

for the zinc-binding core and the loop-rich domain, respectively. The overall RMSD of the backbone atoms to the mean structure of the residues superimposed in Figure 4A and B is 1.5 ± 0.3 and 1.6 ± 0.3 Å, respectively. The quality of the structures is highlighted in Figure 4C and D where the mean structure for each sub-domain has been represented by using a ribbon drawn through the backbone atoms. The individual elements of secondary structure summarized in Figure 1 are generally well defined as summarized in Table 2, which lists the RMS differences for the individual elements of secondary structure and the two β-sheets The good definition of the elements of secondary structure are further evident in Figure 5, a plot of the mean pairwise RMSDs to the mean structure for each residue. Except for the C-terminal region of the helices of both domains, the pairwise RMSD of the backbone atoms to their mean structure rarely rises above 1 Å for residues identified in α-helices, β-sheets or turns in Figure 1. Turn-2 and loop regions r-1 and r-2 have RMSDs near, or above, 1 Å, reflecting a greater amount of flexibility in these regions.

Figure 6 is a model for XPA-MBD based on the average structure calculated for both domains. The relative orientation of the two sub-domains are not well defined since no long range NOEs were confirmed between the zinc-binding core and the loop-rich domain. The lack of interactions between the two sub-domains is reflected in the increase in the pairwise RMSD (Fig. 5) towards the C-terminus of the zinc-binding core, which suggests a region between the two domains is flexible. An elongated, solvent exposed structure is supported by the relatively rapid (4 h) deuterium exchange of all of the backbone $^{1}H^{N}$ resonances.

DISCUSSION

XPA has been shown by filter-binding assays to bind preferentially to UV-, cisplatin- and osmium-tetroxide-damaged DNA over undamaged DNA (26). XPA-MBD has also been shown to have a 4-fold greater affinity for single-stranded DNA over double-stranded DNA (25). As illustrated in Figure 7, XPA also interacts with a number of NER proteins. RPA associates with a region in the minimal DNA binding domain of XPA to form a complex which binds UV-irradiated DNA with a greater affinity than either protein alone and widens the variety of lesions repaired by NER (30). Therefore, XPA-MBD is anticipated to be involved in at least two distinct functions, (i) binding single- and double-stranded DNA and (ii) binding RPA. Our structural investigations indicate that XPA-MBD is 38% helical, 18% β-sheet, 14% turn and 30% unstructured. The predominantly helical nature of XPA-MBD, distributed in four helices, is in accord with the secondary structure estimation made by circular dichroism spectroscopy (31). The absence of assignable long-range NOEs between the two sub-domains, the zinc-binding core and the loop-rich domain, suggest that the two sub-domains are structurally independent in the absence of DNA substrate, XPA residues 1–97 and/or 220–273, or RPA.

Zinc-binding core (D101–K137)

In our previous NMR studies of the zinc-binding core of XPA (zXPA-41), residues V102–C105 and G109–F112 formed an antiparallel β-sheet and residues N128–K137 a nascent α-helix. Even though the zXPA-41 experiments were conducted at pH 6.3 and 25°C (34), rapid exchange of most amide resonances between S115–C126 prevented unambiguous assignment of all the protons resonances in this region. Consequently, a hybrid homology–NMR-based solution structure for zXPA-41 was generated based on similarities in sequence and secondary structure to the zinc-binding domain of the chicken erythroid transcription factor GATA-1 when bound to its cognate DNA target sequence (35). Using the latter technique, a second β-sheet was predicted within residues S115–C126 (34).

The NMR data for XPA-MBD summarized in Figure 1, and the distance geometry/simulated annealing derived calculated structures shown in Figure 4, confirm the presence of the first β-sheet (Y102–C105 and K110–M113) in a region almost identical to that observed in zXPA-41 (V102–C105 and G109–F112). Indeed, the $^{1}H^{\alpha}$ chemical shifts are markedly similar between the residues in the two sequences. The greater number of interstrand NOEs observed for XPA-MBD over zXPA-41 (7 versus 3), together with the detection of slowly exchanging amide resonances for XPA-MBD, results in a better definition of the β-sheet (Fig. 3A). Also observed in the zinc-binding core region of XPA-MBD is an α-helix that extends from C126–K137 (α-1) which overlaps with the residues of the nascent α-helix observed in z-XPA-41 (N128–K137). In contrast with zXPA-41, the α-helix is more stable in XPA-MBD as suggested by the larger number of α-helical NOEs.

The coordination of zinc to the sulfur atom of four Cys residues has been confirmed by EXAFS spectroscopy (38). While structure calculations were performed using Zn–S and S–S distance restraints designed to introduce a tetrahedral geometry between the metal ion and the sulfur atoms; no covalent Zn–S bonds were added into the starting structure. Nevertheless, in all the distance geometry/simulated annealing structures calculated,

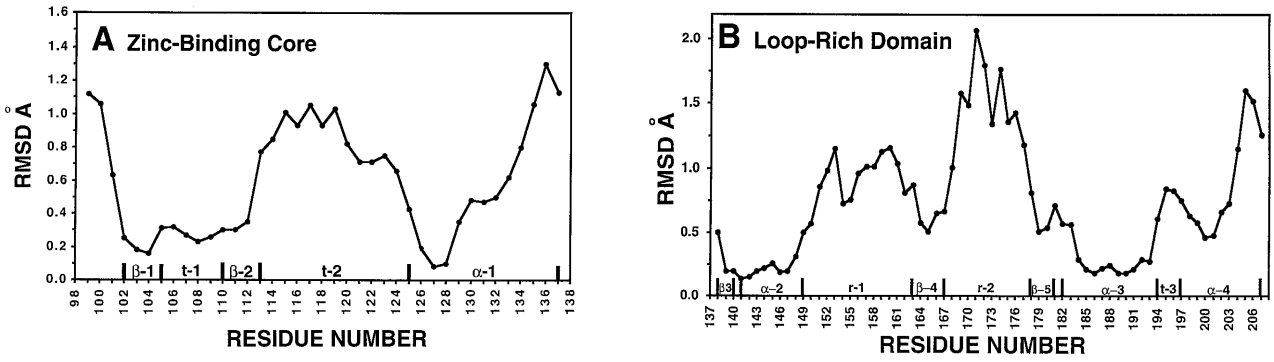

Figure 5. Plots of the mean pairwise RMSDs to the mean structure for each residue of the zinc-binding core (**A**) and the loop-rich domain (**B**). The plots were generated by moving a window of three residues along the sequence and plotting the mean pairwise RMSD (Å) over the central residue.

an R configuration (using priorities assigned C126 > C105 > C129 > C108) of the Cys sulfur atoms about the zinc (51) was generated. Figure 4C illustrates the R orientation of the four Cys residues around the zinc with C105 and C108 in a turn (t-1) of the antiparallel β-sheet (β-1/β-2) and C126 and C129 part of a helix (α-1). It is interesting to note that all four zinc-coordinated Cys $^1H^N$ resonances exchange very slowly with D_2O. While the $^1H^N$ resonance of C105 exchanges slowly because it is in a β-sheet (Fig. 3A), the other three slowly exchanging Cys amide resonances suggest a structure about the metal ion that may be stabilized by a unique network of hydrogen bonds between the backbone $^1H^N$ groups and the sulfur atoms of the Cys residues coordinated to the zinc, as observed in the case of rubredoxin from *Pyrococcus furiousus* which contains a C–X–X–C–G–X metal binding motif (52,53). The average structure of the zinc-binding core indicates that three of the four cysteine residues have $^1H^N$–S distances of ~2.5 Å. However, the N, $^1H^N$, S bond angle is ~90°, which is less than the minimum angle of 120° necessary for ideal hydrogen bond formation (46). Further experiments to determine if the Cys amide protons are coupled to ^{113}Cd via hydrogen bonds with the Cys sulfur atoms will be necessary to define the precise hydrogen bonding interactions involving the Cys amide protons.

One significant difference between the zinc-binding core region of zXPA-41 and XPA-MBD is that all the amide resonances between S115–C126 are observed in the larger XPA fragment studied here, even though the pH (7.3 versus 6.2) and temperature (30 versus 25°C) are elevated. Consequently, more NOEs for residues D101–K141 are observed in XPA-MBD over zXPA-41. Such observations suggest that the addition of 82 C-terminal residues to the zinc-binding core of zXPA-41 effects a structural stabilization of the identical region in XPA-MBD. Using the NMR data in Figure 1 and the distance geometry/simulated annealing derived structures in Figure 4, it is now possible to define more accurately the secondary structure of residues S115–T125 in XPA even though the pairwise RMSDs (Fig. 5) of the residues in this region suggest that this turn is flexible. Foremost, the absence of long-range $^1H^N_i$ to $^1H^N_j$ and $^1H^\alpha_i$ to $^1H^\alpha_j$ NOEs between the extremities of the S115–T125 region disproves the β-sheet predicted previously in the region using hybrid homology–NMR modelling (34). Instead, the S115–T125 region in XPA-MBD, at least in the absence of DNA, adopts a structure that contains a single turn of an α-helix followed by a tight turn as illustrated in the distance geometry/simulated annealing derived structures (Figs. 4 and 6). Three i to i+3 and i+4 NOEs between S115 to M118 and N119 are consistent with the formation of a single turn of an α-helix involving residues S115–N119 and negative consensus CSI values for Y116–N119 further support such an interpretation (Fig. 1). However, the lack of a full complement of i to i+3 and i+4 NOEs over the entire S115–T125 region (Fig. 1) indicate that it is not entirely helical as others have predicted using a 3D–1D compatibility analysis method (54).

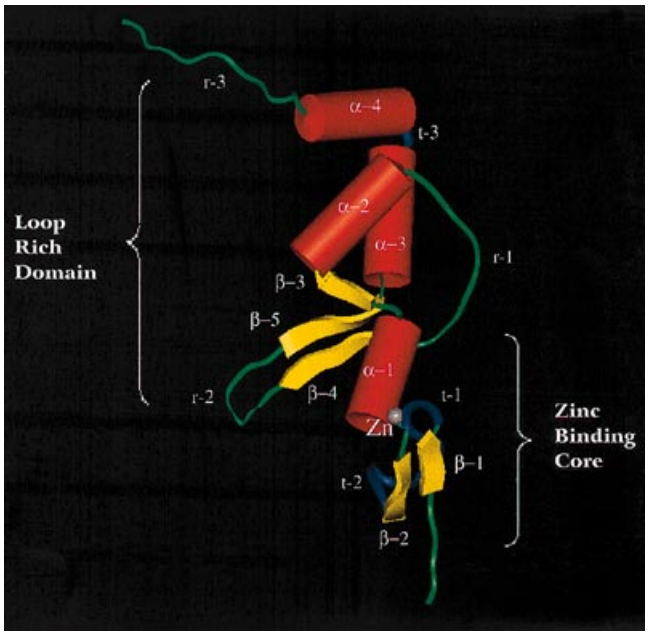

Figure 6. A three-dimensional model of XPA-MBD obtained by linking the average distance geometry/simulated annealing calculated structures of the zinc-binding core to the loop-rich domain. Red, α-helix; yellow, β-sheet; blue, turn; green, random coil.

The loop-rich domain (L138–F219)

While the zinc-binding core is essential for binding DNA, as shown by the reduction in DNA binding activity upon (i) the

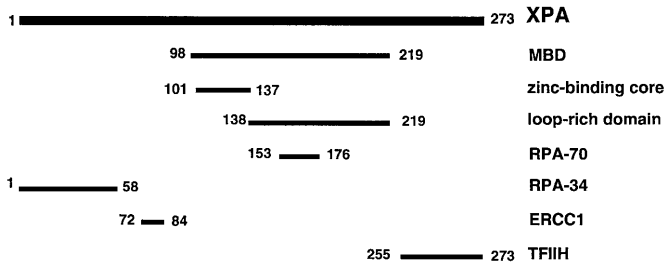

Figure 7. Map of the functional regions of XPA.

removal of zinc and (ii) the replacement of C105, C108, C126 or C128 with a Ser in experiments on XPA (17), the core structure alone (D101–K137) does not bind DNA (31). An additional 82 residues (L138–F219), corresponding to the loop-rich domain, are required for DNA binding. As illustrated in Figures 4 and 6, the loop-rich domain consists of a triple-strand antiparallel β-sheet, three α-helices and three loops. The three helices form a loose bundle that is orientated perpendicular to the triple-strand β-sheet with loops joining β-4 to β-5 and α-2 to β-4. The ability of XPA to bind DNA is lost in an XPA fragment that is terminated at W194 (S49–W194) (31). The C-terminal 26 residues of XPA-MBD (W194–F219) have been predicted to adopt a helical conformation (31). We observe that Q197–R207 (α-4) does indeed form an α-helix; however, the remaining residues between Q208 and F219 (r-3) are disordered. The absence of a complete helix at the C-terminus may be due to termini dynamic fraying, truncation of the full-length XPA protein, the absence of other NER proteins, or the absence of a DNA substrate.

Approximately 30% of XPA-MBD is unstructured and the majority (90%) of this disorder is in the loop-rich domain. Given XPA's ability to associate with both single- and double-stranded DNA, such flexibility may be expected in the absence of a damaged DNA substrate. Furthermore, it is plausible that the structure of XPA might change, not only upon association with DNA, but also upon association with other proteins (Fig. 7) involved in NER (55). The 70 kDa subunit of RPA is the only NER protein that is known to bind to XPA-MBD and is required for XPA to function in complementation of XP-A cells in a UV survival assay (56). The location of RPA-70 binding to XPA-MBD has been pinpointed to a 24 residue region (C153–G176) located in r-2 in the loop-rich domain of XPA-MBD (Fig. 7) (56). Unstructured regions in isolated proteins have been shown to play a role in protein–protein interactions (57,58). Therefore, r-2, as well as r-1 and r-3, may be involved in the conformational changes that occur to XPA upon association with the NER proteins and/or damaged DNA.

Possible mechanisms for DNA binding

Zinc binding motifs play an important role in gene regulation with at least ten different classes having been characterized (59), five of which bind to DNA (60,61). XPA appears to be a class IV zinc-dependent DNA binding protein, associating with DNA as a monomer through a single, C-4 motif of the form $C–X_2–C–X_{17}–C–X_2–C$ (10,26). The erythroid transcription factor GATA-1 is the prototypical member of the class IV zinc-dependent DNA binding proteins (62). The NMR solution structure of the DNA binding domain of the chicken erythroid transcription factor, cGATA-1 (K158–R223), has been determined bound to its cognate DNA substrate (35). The structure has been described as a 'hand (protein) holding a rope (DNA)' with the 'hand' composed of two functional regions, the 'palm and fingers' [38 residue zinc-binding core (K158–H195)] and a 'thumb' [28 residue C-terminal (Q196–R223)]. The zinc-binding core provides a scaffold for binding double-stranded DNA, interacting specifically with nucleotide bases in the major groove and non-specifically with the DNA sugar–phosphate backbone. The C-terminal 'thumb' confers further specificity to the DNA binding, wrapping itself into the DNA minor groove (35).

While cGATA-1 and XPA-MBD share some structural similarities, at this time there is no clear functional analogy between the two proteins. Only one of the two sub-domains of XPA-MBD is structurally comparable with cGATA-1, the zinc-binding core and the 'palm and fingers'. Both sub-domains contain a β-sheet between the first two zinc-associated Cys residues and an α-helix containing the second two zinc-associated Cys residues. The major difference between the two zinc-chelated core structures is the presence of a turn (t-1) within XPA-MBD residues S115–T125 instead of the second β-sheet observed in the analogous region in cGATA-1. It is possible that the loop (t-1) in XPA-MBD may change structure upon binding DNA and the function of the zinc-binding domain, like in cGATA-1, may be to serve as a scaffold for double-helical DNA. However, initial $^{15}N/^{1}H$ two-dimensional HSQC chemical shift mapping experiments suggest that the structure of the zinc-binding core is unperturbed by the addition of a damaged single- or double-stranded DNA substrate (G.W.Buchko and M.A.Kenedy, unpublished results).

While the zinc-binding core of the XPA-MBD and cGATA-1 are the same size and share similar structural features, the C-terminal sub-domains of both proteins differ significantly. XPA requires a larger region, 82 residues at the C-terminus of the zinc-associated core, to bind damaged DNA, while cGATA-1 requires only 28 residues (the 'thumb') at the C-terminus of the zinc-associated core to recognize its cognate DNA substrate. In cGATA-1, the C-terminus wraps around its DNA substrate, while in XPA-MBD the C-terminus forms a structure containing a triple-strand β-sheet and a three helix bundle interspaced with three loops (Fig. 6). It is not surprising that the structural similarities diverge given the distinct functional roles of XPA and cGATA-1. For example, cGATA-1 recognizes a specific, double-stranded DNA sequence and binds tightly to it (35), whereas XPA-MBD participates in the recognition of an extensive list of DNA lesions that are corrected by NER. The list, as determined by *in vitro* and *in vivo* investigations, includes bulky adducts of benzo[a]pyrene, acetylaminofluorene, aflatoxin, chlorestorol, psoralen, cross-linked cisplatin adducts, UV-induced lesions such as cyclobutane pyrimidine dimers and the [6–4] photoproduct, apurinic sites, oxidative lesions and G:G mismatches (1,63,64). According to the prevailing model, the topological feature recognized by XPA in the aforementioned list of DNA lesions is single-stranded character leading to an 'open complex formation' (6,25,29). Preliminary chemical shift mapping experiments with RPA and single- and double-stranded DNA indicate that the RPA interactions are spread throughout both domains with slightly more perturbations to the zinc-binding core whereas the DNA interactions are highly localized in the loop-rich domain (G.W.Buchko, D.F.Lowry, B.K.Sudha Rao and M.A.Kennedy, unpublished results). Consequently, despite the presence of a

similar zinc-binding core in cGATA and XPA, the mechanism of DNA binding probably differs significantly between cGATA-1 and XPA.

CONCLUSIONS

XPA is the only known eukaryotic DNA repair protein to contain a C4-type zinc-associated DNA binding domain. Two other bacterial DNA repair proteins, UvrA (65) and fapy-DNA-glycosylase (66) also contain the C-4 motif. Bacterial UvrA, which binds damaged DNA as a dimer, contains two C-4 type zinc-binding motifs and requires a helix–turn–helix motif to recognize its damaged substrate (67). Bacterial fapy-DNA-glycosylase contains a single C-4 type zinc binding motif but it is located at the very end of the C-terminus. Hence, the structural organization of the minimal DNA binding domain of XPA appears to be unique among DNA repair proteins. The presence of two structurally distinct sub-domains together with preliminary chemical shift mapping experiments indicate that the two primary functional roles of XPA-MBD may be divided according to its structural organization into two distinct regions, a zinc-binding core and the loop-rich domain. The unstructured or loop regions may represent the structural features required to facilitate the reorganization of XPA necessary to accommodate binding to DNA and RPA.

ACKNOWLEDGEMENTS

We thank Dr David F. Lowry for helpful discussions and Dr Chaunlinag Liu for collection and analysis of mass spectrometric data. This work was performed under the auspices of the US Department of Energy (Contract DE-AC06-76RLO1830) and was supported by the Department of Energy Office of Biological and Environmental Research Program, under Grant 249311 KP11-01-01. G.W.B. and S.N. were supported by Associated Western Universities, Inc., Northwest Division (AWU-NW) under Grant DE-FG06-92RL-12451 with the US Department of Energy.

See supplementary material available in NAR Online. A table containing the the ^{15}N, $^{13}C^{\alpha}$, $^{13}C^{\beta}$, ^{13}CO, $^{1}H^{N}$, $^{1}H^{\alpha}$ $^{1}H^{\beta}$, and $^{1}H^{other}$ chemical shifts are available from the authors by mail.

REFERENCES

1 Huang,J.-C., Hsu,D.S., Kazantzev,A. and Sancar,A. (1994) *Proc. Natl. Acad. Sci. USA*, **91**, 12213–12217.
2 Tanaka,K. and Wood,R.D. (1994) *Trends Biochem. Sci.*, **19**, 83–86.
3 Naegeli,H. (1995) *FASEB J.*, **9**, 1043–1050.
4 Friedberg,E.C., Walker,G.C. and Siede,W. (1995) *DNA Repair and Mutagenesis*. American Society for Microbiology, Washington, DC, pp. 283–365.
5 Sancar,A. (1995) *J. Biol. Chem.*, **270**, 15915–15918.
6 Gunz,D., Hess,M.T. and Naegeli,H. (1995) *J. Biol. Chem.*, **271**, 25089–25098.
7 Wood,R.D. (1997) *J. Biol. Chem.*, **272**, 23465–23468.
8 Huang,J.-C., Svoboda,D.L., Reardon,J.T. and Sancar,A. (1992) *Proc. Natl. Acad. Sci. USA*, **89**, 3663–3668.
9 Cleaver,J.E. and Kraemer,K.H. (1989) In Scriver,S.C., Beaudet,A.L., Sly,W.S. and Valle,D. (eds), *The Metabolic Basis of Inherited Disease*. McGraw-Hill Book Co., New York, NY.
10 Tanaka,K., Miura,N., Satokata,I., Miyamoto,I., Yoshida,M.C., Satoh,Y., Kondo,S., Yasui,A., Okayama,H. and Okada,Y. (1990) *Nature*, **348**, 73–76.
11 Weeda,G., van Ham,R.C.A., Vermeulen,W., Bootsma,D., van der Eb,A.J. and Hoeijmakers,J.H.J. (1990) *Cell*, **62**, 777–791.
12 Legerski,R.J. and Peterson,C. (1992) *Nature*, **359**, 70–73.
13 Masutani,C., Sugasawa,K., Yanagisawa,J., Sonoyama,T., Ui,M., Enomoto,T., Takio,K., Tanaka,K., van der Spek,P.J., Bootsma,D., Hoeijmakers,J.H.J. and Hanaoka,F. (1994) *EMBO J.*, **13**, 1831–1843.
14 Flejter,W.L., McDaniel,L.D., Johns,D., Friedberg,E.C. and Schultz,R.A. (1992) *Proc. Natl. Acad. Sci. USA*, **89**, 261–265.
15 O'Donovan,A. and Wood,R.D. (1993) *Nature*, **363**, 185–188.
16 Scherly,D., Nouspikel,T., Corlet,J., Ucla,C., Bairoch,A. and Clarkson,S.G. (1993) *Nature*, **363**, 182–185.
17 Miyamoto,I., Miura,N., Niwa,H., Miyazaki,J. and Tanaka,K. (1992) *J. Biol. Chem.*, **267**, 12182–12187.
18 Shimamoto,T., Kohno,K., Tanaka,K. and Okada,Y. (1991) *Biochem. Biophys. Res. Commun.*,**181**, 1231–1237.
19 Li,L., Elledge,S.J., Peterson,C.A., Bales,E.S. and Legerski,R.J. (1994) *Proc. Natl. Acad. Sci. USA*, **91**, 5012–5016.
20 Park,C.-H. and Sancar,A. (1994) *Proc. Natl. Acad. Sci. USA*, **91**, 5017–5021.
21 Park,C.-H., Mu,D., Reardon,J.T. and Sancar,A. (1995) *J. Biol. Chem.*, **270**, 4896–4901.
22 Nocentini,S., Coin,F., Saijo,M., Tanaka,K. and Egly,J.-M. (1997) *J. Biol. Chem.*, **272**, 22991–22994.
23 Matsuda,T., Saijo,M., Kuraoka,I., Kobayashi,T., Nakatsu,Y., Nagai,A., Enjoji,T., Masutani,C., Sugasawa,K., Hanoaka,F., Yasui,A. and Tanaka,T. (1995) *J. Biol. Chem.*, **270**, 4152–4157.
24 Robins,P., Jones,C.J., Biggerstaff,M., Lindahl,T. and Wood,R.D. (1991) *EMBO J.*, **10**, 3913–3921.
25 Jones,C.J. and Wood,R.D. (1993) *Biochemistry*, **32**, 12096–12104.
26 Asahina,H., Kuraoka,I., Shirakawa,M., Morita,E.H., Miura,N., Miyamoto,I., Ohtsuka,E., Okada,Y. and Tanaka,K. (1994) *Mutat. Res.*, **315**, 229–238.
27 Coverley,D., Kenny,M., Munn,M. Rupp,W.D., Lane,D.P. and Wood,R.D. (1991) *Nature*, **349**, 538–541.
28 Satoh,M.S., Jones,C.J., Wood,R.D. and Lindahl,T. (1993) *Proc. Natl. Acad. Sci USA*, **90**, 6335–6339.
29 Evans,E., Fellows,J., Coffer,A. and Wood,R.D. (1997) *EMBO J.*, 16, 625–638.
30 He,Z., Henrickson,L.A., Wold,M.S. and Ingles,C.J. (1995) *Nature*, **374**, 566–569.
31 Kuraoka,I., Morita,E.H., Saijo,M., Matsuda,T., Morikawa,K., Shirakawa,M. and Tanaka,K. (1996) *Mutat. Res.*, **362**, 87–95.
32 Berg,J.M. (1990) *J. Biol. Chem.*, **265**, 6513–6516.
33 Klug,A. and Schwabe,W.R. (1995) *FASEB J.*, **9**, 597–604.
34 Buchko,G.W. and Kennedy,M.A. (1997) *J. Biomol. Struct. Dyn.*, **14**, 677–690.
35 Omichinski,J.G., Clore,G.M., Schaad,O., Felsenfeld,G., Trainor,C., Appella,E., Stahl,S.J. and Gronenborn,A.M. (1993) *Science*, **261**, 438–446.
36 Buchko,G.W., Ni,S., Thrall,B.D. and Kennedy,M.A. (1997) *J. Biol. NMR*, **10**, 313–314.
37 Kay,L.E. (1997) *Biochem. Cell Biol.*, **75**, 1–15.
38 Hess,N.J., Buchko,G.W., Conradson,S.D., Espinosa,F.J., Ni,S., Thrall,B.D. and Kennedy,M.A. (1998) *Protein Sci.*, in press.
39 Kay,L.E., Keifer,P. and T.Saarinen (1992) *J. Am. Chem. Soc.*, **114**, 10663–10665.
40 Zhang,O., Kay,L.E., Olivier,J.P. and Forman-Kay,J.D. (1994) *J. Biol. NMR*, **4**, 845–858.
41 Yamazaki,T., Lee,W., Revington,M., Mattiello,D.L., Dahlquist,F.W., Arrowsmith,C.H. and Kay, L.E. (1994) *J. Am. Chem. Soc.*, **116**, 6464–6465.
42 Muhandiram,D.R. and Kay,L.E. (1994) *J. Magn. Reson. B*, **103**, 203–216.
43 Kay,L.E., Xu,G.-Y., Singer,A.U., Muhandiram,D.R. and Forman-Kay,J.D. (1993) *J. Magn. Reson. B*, **101**, 333–337.
44 Grzesiek,S., Anglister,J. and Bax,A. (1993) *J. Magn. Reson. B*, **101**, 114–119.
45 Kay,L.E. and Bax,A. (1990) *J. Magn. Reson.*, **86**, 110–126.
46 Rozek,A., Buchko,G.W. and Cushley,R.J. (1995) *Biochemistry*, **34**, 7401–7408.
47 Wishart,D.S., Sykes,B.D. and Richards,F.M. (1992) *Biochemistry*, **31**, 1647–1651.
48 Wishart,D.S., Bigam,C.G., Holm,A., Hodges,R.S. and Sykes,B.D. (1995) *J. Biomol. NMR*, **5**, 67–81.
49 Wüthrich,K. (1986) *NMR of Proteins and Nucleic Acids*. John Wiley & Sons, New York, NY.
50 O'Neil,K.T. and DeGrado,W.F. (1990) *Science*, **250**, 646–651.
51 Berg,J. (1988) *Proc. Natl. Acad. Sci. USA*, **85**, 99–102.
52 Blake,P.R., Park, J.B., Adams,M.W.W. and Summers,M.F. (1992) *J. Am. Chem. Soc.*, **114**, 4931–4933.

53 Blake,P.R., Lee,B., Summers,M.F., Adams,M.W.W., Park,J.-B., Zhou,Z.H. and Bax,A. (1992) *J. Biol. NMR*, **2**, 527–533.
54 Morita,E.H., Ohkubo,T., Kuraoka,I., Shirakawa,M., Tanaka,K. and Morikawa,K. (1996) *Genes Cells*, **1**, 437–442.
55 Saijo,M., Kuraoka,I., Masutani,C., Hanaoka,F. and Tanaka,K. (1996) *Nucleic Acids Res*., **24**, 4719–4724.
56 Li.,L., Lu,X., Peterson,C.A. and Legerski,R.J. (1995) *Mol. Cell. Biol*., **15**, 5396–5402.
57 Schulz,G.E. (1977) *Molecular Mechanism of Biological Recognition*. Elsevier North Holland Biomedical Press, pp. 79–94.
58 Stites,W.E. (1997) *Chem. Rev.*, **97**, 1233–1250.
59 Schwabe,J.W.R. and Klug,A. (1995) *Nature Struct. Biol*., **1**, 345–360.
60 Harrison,S.C. (1991) *Nature*, **353**, 715–719.
61 Berg,J.M. and Shi,Y. (1996) *Science*, **271**, 1081–1085.
62 Ho,I.C., Vorhees,P., Marin,N., Oakley,B.K., Tsai,S.-F., Orkin,S.H. and Leiden,J.M. (1991) *EMBO J*., **10**,. 1187–1192.
63 Cleaver,J.E. (1973) *Cancer Res*., **33**, 362–369.
64 Wang,G., Seidman,M.M. and Glazer,P.M. (1996) *Science*, **271**, 802–805.
65 Navaratnam,S., Myles,G.M., Strange,R.W. and Sancar,A. (1989) *J. Biol. Chem*., **264**, 16067–16071.
66 Tchou,J., Michaels,M.L., Miller,J.H. and Grollman,A.P. (1993) *J. Biol. Chem*., **268**, 26738–26744.
67 Wang,J. and Grossman,L. (1993) *J. Biol. Chem*., **268**, 5323–5331.